Applied Physics A (2022) 128:29
https://doi.org/10.1007/s00339-021-05182-5

Applied Physics A
Materials Science & Processing

Fabrication of mesoporous CeO_2–MgO adsorbent with diverse active sites via eggshell membrane-templating for CO_2 capture

Amirul Hafiiz Ruhaimi[1] · **Muhammad Arif Ab Aziz**[1,2]

Received: 11 August 2021 / Accepted: 2 December 2021 / Published online: 10 December 2021

Abstract
There is an increasing demand for the development of highly efficient CO_2 capture techniques to address global warming and climate change. Although adsorption is an effective approach towards capturing CO_2, conventional adsorbents possess limited adsorption capacities and exhibit low adsorption rates. In this study, we successfully fabricated mesoporous composite CeO_2–MgO adsorbents (CM-BT) with diverse active sites via the eggshell membrane (ESM)-templating method, for CO_2 capture applications. The utilisation of ESM-templating produced a CM-BT with better structural and textural properties. The CM-BT possessed a higher surface area (42 m^2/g) and pore volume (0.185 cm^3/g) than those of the composite prepared using a thermal decomposition method (CM-TD). In addition, the CM-BT possessed more diverse base sites of various strong base site strengths (O^{2-}) and abundant hydroxyl groups, and metal–oxygen pair base sites than CM-TD. The diverse strengths of the strong base sites were correlated with the coordination of O^{2-} and the electronegativity of metal ions. With these excellent physicochemical properties, the CM-BT composite exhibited a high CO_2 uptake capacity of 5.7 mmol/g under CO_2 flow and ambient conditions, which is 2.5 times higher than that of CM-TD.

1 Introduction

The combustion of fossil fuels for energy generation is the primary source of greenhouse gas (GHG) emissions [1]. The continued utilisation of fossil fuels could result in an increase in the atmospheric concentrations of GHGs, such as carbon dioxide (CO_2), and further contribute to severe global warming and climate change [2, 3]. Hence, to achieve the United Nations Sustainable Development Goals (UNSDGs) pertaining to sustainability and climate action, a carbon capture approach is needed to minimise GHG emissions. Several techniques, such as cryogenic distillation, membrane separation, absorption, and adsorption, can be used to capture CO_2. Currently, the absorption process is the most widely used technique for CO_2 capture. However, owing to the disadvantages of this technique, such as poor sorbent stability, high equipment corrosion rate, solvent (amine) degradation, and high regeneration costs [4], thus the adsorption process seems to be considered as a better candidate for capturing CO_2. Adsorption process possess several advantages such as durable and economical solid adsorbent, easy handling and recovery, and low regeneration energy requirement [5]. Moreover, the loss of amine during the absorption process and its emission into the environment can be harmful to both human health and the environment [6].

CO_2 adsorption can be achieved using several types of adsorbents, such as zeolites, porous carbon, organic frameworks, silica, and metal oxides. However, conventional adsorbents tend to suffer from limited adsorption capacities and low adsorption rates [7]. Therefore, it is desirable to fabricate adsorbents with excellent physicochemical properties that may contribute to improving their adsorption performance. Metal-oxide-based adsorbents like magnesium oxide (MgO) have attracted significant interest because of their promising properties, such as high theoretical adsorption capacity (1.09 g of CO_2 per gram of MgO), a wide temperature range for CO_2 capture, wide availability of magnesium, and low toxicity [5]. In addition, composite MgO adsorbents have attracted much attention because they offer high surface basicity, resulting in high CO_2 uptake capacity.

✉ Muhammad Arif Ab Aziz
m.arif@utm.my

[1] School of Chemical and Energy Engineering, Faculty of Engineering, Universiti Teknologi Malaysia (UTM), UTM Johor Bahru, 81310 Johor, Malaysia

[2] Centre of Hydrogen Energy, Institute of Future Energy, Universiti Teknologi Malaysia (UTM), UTM Johor Bahru, 81310 Johor, Malaysia

For instance, a composite of MgO and CeO_2 exhibited an enhanced adsorbent surface reactivity owing to the generation of surface oxygen vacancies. According to Liu et al., this reactivity is correlated with the synergetic effect between CeO_2 and other doped metal oxides such as MgO [8]. This effect facilitates ion exchange between M^{n+}/M^{n+1} and Ce^{3+} and Ce^{4+}, which generates active sites for trapping CO_2. This is supported by the findings of a study conducted by Yu et al., where a composite MgO–CeO_2 adsorbent exhibited higher surface basicity than pure MgO and another MgO composite (MgO–Al_2O_3), thus demonstrating a higher CO_2 uptake capacity [9]. As mentioned, the excellent CO_2 uptake capacity of the adsorbent is influenced by its textural and structural properties. To this end, numerous synthesis approaches have been developed to enhance these properties of adsorbents.

Several techniques, such as flame aerosol synthesis, urea hydrolysis, solid-state reaction, precipitation, water-to-oil emulsification, hydrothermal, and solvothermal pyrolysis methods, have been used to fabricate adsorbents with excellent physicochemical properties [5]. However, each method has its own disadvantages. For example, although MgO with ultra-high surface area (350–500 m^2/g) has been fabricated via the aerogel and chemical vapour deposition methods, these methods require extreme conditions (temperature and pressure) and expensive equipment [10]. In addition, surfactants such as triblock copolymer (P123), sodium dodecyl sulphate (SDS), and cetyltrimethylammonium chloride (CTAC) are utilised for the synthesis of high-surface-area adsorbents. However, such methods using surfactants are expensive because of the high cost of surfactant templates and complex synthesis procedures [5]. Therefore, an alternative approach for replacing the surfactant template in the synthesis of high-surface-area adsorbents is the utilisation of a bio-material as a template, also known as the bio-templating method.

Several studies have been conducted using bio-templating methods, such as by using cotton fibres, root hair, jute root, rose petals, and eggshell membranes (ESMs), to fabricate metal oxide samples [5]. Each bio-template possesses unique characteristics. For instance, ESMs are composed of several different surface functional groups, such as carboxyl (–COOH), amine (–NH_2), and hydroxyl (–OH) groups, which provide them with a strong ability to bind and capture metal ions during the preparation stage. Moreover, ESMs comprise collagen and glycoproteins, which form an interwoven three-dimensional fibrous network structure [11]. Previous reports have stated that the fabricated ESM-metal oxide preserves the parental ESM used [11, 12]. This enhanced the textural and structural properties of the adsorbent, and hence, is expected to improve its CO_2 uptake performance. However, there are very few studies on the effect of the bio-templating method on the CO_2 adsorption performance of the adsorbents.

In this study, a mesoporous CeO_2–MgO composite was prepared via the bio-templating method with an ESM as the template. For comparison, another composite CeO_2–MgO adsorbent was synthesised via the thermal decomposition method. The surface and structural characteristics of the adsorbents were analysed by X-ray powder diffraction (XRD) analysis, nitrogen (N_2) physisorption, Fourier-transform infrared spectroscopy with potassium bromide (FTIR-KBr), CO_2 temperature-programmed desorption (CO_2-TPD), field-emission scanning electron microscopy (FESEM), and transmission electron microscopy (TEM). The prepared adsorbents were evaluated during the adsorption process, at ambient pressure and temperature under pure CO_2 flow, to understand the relationship between the physicochemical properties and the uptake capacity of the adsorbent.

2 Experimental

2.1 Material

The ESM used in this study was obtained from a local market. Ammonia solution (NH_3, 28%), ethylene glycol ($C_2H_6O_2$) (EG), and magnesium nitrate hexahydrate ($Mg(NO_3)_2{\cdot}6H_2O$) were purchased from QRëC. Cerium (III) chloride heptahydrate ($CeCl_3{\cdot}7H_2O$, 99%) was purchased from Acros Organics. All the reagents were of analytical grade.

2.2 Preparation of CeO_2–MgO adsorbent by thermal decomposition

$CeCl_3{\cdot}7H_2O$ and $Mg(NO_3)_2{\cdot}6H_2O$ were mixed in a molar ratio of 0.75:0.25 and preheated at 383 K for 1 h. The preheated sample was then calcined at 873 K for 3 h and ground prior to adsorption testing. This adsorbent is denoted by CM-TD.

2.3 Preparation of CeO_2–MgO adsorbent via eggshell membrane bio-templating

In this method, ESMs were carefully peeled off from the eggshell waste and rinsed thrice using distilled water to remove any impurities. The rinsed ESMs were dried overnight at 383 K and cut into small pieces (approximately less than 0.25 cm^2) before being used in the templating method. $Mg(NO_3)_2{\cdot}6H_2O$ and $CeCl_3{\cdot}7H_2O$ were taken in a molar ratio of 0.75:0.25 and dissolved in 200 mL of EG. The solution was stirred and sonicated for 10 min until the magnesium and cerium salts dissolved completely. Dried ESM (3 g) was immersed in this solution and stirred for 1 h

at 298 K, followed by adjusting the solution pH to 10 using an NH_3 solution. Subsequently, the solution was stirred for 30 min. The adsorbed ESM was filtered and dried at 383 K for 1 h, followed by calcination at 772 K for 3 h, and ground to form a powder. The as-prepared adsorbent is denoted by CM-BT.

2.4 Characterisation

The morphological features of the samples were characterised by FESEM and energy-dispersive X-ray (EDX) analysis (ZEISS Crossbeam 340), and high-resolution transmission electron microscopy (HRTEM, JEOL JEM-ARM 200F). EDX was used for elemental mapping analysis. The textural properties were evaluated from the N_2 adsorption/desorption isotherms obtained using Autosorb IQ (version 3.0) from Quantachrome Instruments. XRD analysis of the adsorbent samples was conducted using an X-ray diffractometer (Rigaku SmartLab) operated at 40 kV and 100 mA with Cu Kα radiation ($\lambda = 1.5418$ Å). FTIR spectroscopy was performed using an ATR Shimadzu-IR Tracer over a mid-infrared range from 400 to 4000 cm^{-1}. The CO_2 temperature-programmed desorption (CO_2-TPD) profiles of the samples were recorded using AutoChem II 2920 (V4.03) from Micromeritics instrument to identify the active sites of the adsorbent. The decomposition behaviour of the adsorbent was elucidated by thermogravimetric analysis (TGA) in the temperature range 303–1273 K with a ramping rate of 10 K/min, using a PerkinElmer STA 8000 instrument.

2.5 CO_2 adsorption measurement

The CO_2 adsorption/desorption measurements were conducted using a fixed-bed U-shaped adsorption column equipped with a CO_2 analyser (Quantek Instrument Model 906). The adsorption was evaluated at 1 bar and 303 K. The adsorbent (0.05 g) was inserted into the adsorption column and then pre-treated at 423 K by immersing it into the heated silicone oil for 30 min under N_2 flow (20 mL/min). The adsorption process was carried out under CO_2 flow (10 mL/min) for 1 h. For the desorption process used in evaluating the adsorbed amount of CO_2 by the adsorbent, the adsorption column was immersed into the heated silicone oil (423 K) under N_2 flow to initiate the desorption process, and the condition was maintained around 30 min–1 h until the CO_2 was fully desorbed. The desorbed CO_2 from the adsorbent was quantified using the area under the curve generated from the desorption process. With the aim of studying the practicality of the prepared sample over several adsorption processes, the cyclic adsorption–desorption process was conducted. The cyclic testing was conducted under the same condition for both samples with five adsorption–desorption cycles.

3 Results and discussion

3.1 Characterisation

The morphological features of both the CM adsorbents, as observed via FESEM, are shown in Fig. 1. Owing to the use of the ESM bio-templating method, the morphological features of CM-BT were different from those of CM-TD. CM-BT featured nano-sized CeO_2 with rod-like Mg (Fig. 1b). In contrast, the CM-TD adsorbent displayed a mixture of irregular crystallites and spherical structures (Fig. 1a). The rod-like structure observed in Fig. 1b was confirmed to be Mg by EDX elemental mapping (Fig. 1h). While CM-TD's Mg element was scattered throughout the adsorbent (Fig. 1d). However, preservation of parental ESM was not observed in the prepared samples.

The ESM bio-templating method was utilised in this study to generate a CM adsorbent with enhanced structural and textural properties, which ultimately affect the CO_2 uptake capacity of the adsorbent. EG is one of the factors that influence the physicochemical properties of the adsorbent. EG has been reported to be a promising chelating agent for metal oxides because of its two hydroxyl (-OH) groups [13]. Chelation is the formation of bonds between two or more binding sites within the same ligand (an organic compound called chelant, chelator, or chelating agent) and a single central atom [14]. The chelation process might have occurred during the dissolution of the metal salts (cerium chloride and magnesium nitrate) in EG, and the mechanism of formation is proposed as follows:

$$\left(CH_2OH\right)_2 + Mg\left(NO_3\right)_2 \rightarrow Mg\left(OCH_2\right)_2 + 2HNO_3 \quad (1)$$

$$3\left(CH_2OH\right)_2 + 2CeCl_3 \rightarrow 2Ce\left(OCH_2\right)_3 + 6HCl \quad (2)$$

In this study, the chelation process resulted in the formation of chelated compounds, i.e. magnesium ethylene glycolate ($Mg(OCH_2)_2$) and cerium ethylene glycolate ($Ce(OCH_2)_2$). This is in line with the findings of a study conducted by Li et al., where magnesium ions formed a metal-polyol chelated structure by the solvothermal process [7, 15]. This formation then transformed into a MgO-based adsorbent with outstanding morphological features (flower-like shape), contributing to the high CO_2 uptake capacity. However, in this study, a rod-like Mg-based adsorbent was formed instead of a flower/sheet-like structure, as reported in other papers [7, 15]. This might be influenced by the generation of intermediate compounds with different structural memories than those reported in the literature. In addition, this rod-like structure can be attributed to the presence of other Mg-based compounds,

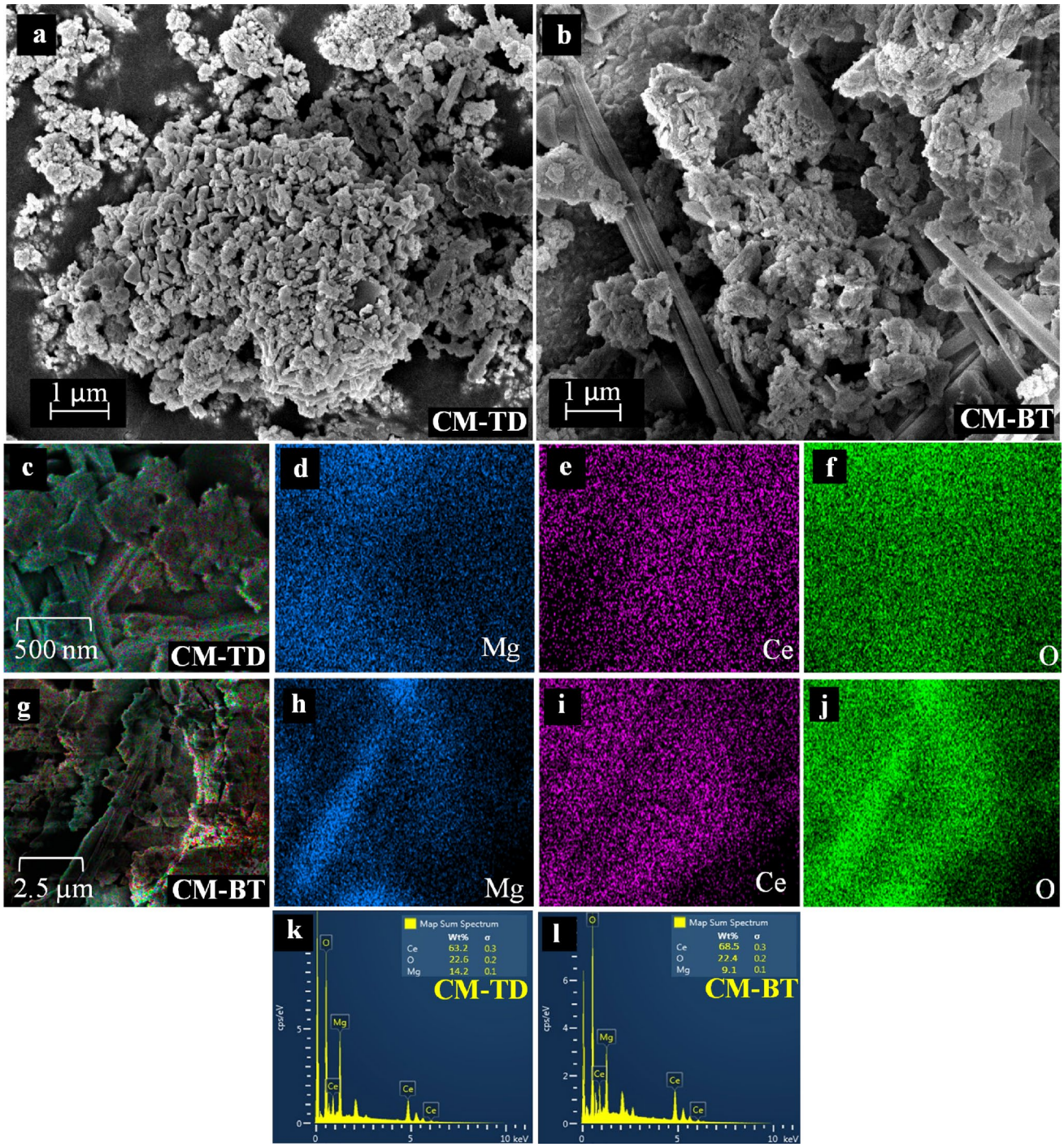

Fig. 1 **a**, **b** FESEM images, **c**–**j** EDX elemental mapping, and **k**, **l** EDX point ID of CM-TD and CM-BT

such as nesquehonite, in the adsorbent [16]. This is supported by the XRD pattern (Fig. 3), which indicates the presence of several Mg-based compounds in the CM-BT adsorbent.

In addition, as reported by Osaki et al., cerium ions are able to form a chelated compound (cerium ethylene glycolate) in the presence of EG [13]. In their study, CeO_2 generated on an aluminium support after calcination exhibited a fine particle size, and these particles were found to be highly dispersed on the surface of the support. These highly dispersed fine CeO_2 particles demonstrated higher catalytic activity than CeO_2–Al_2O_3 synthesised without EG utilisation. In which support the finding on the CM-BT sample, where Ce observed highly dispersed through the adsorbent

as demonstrated in Fig. 1i than CM-TD (Fig. 1e). These than further supported by the EDX point ID (Fig. 1k, l), that CM-BT possess higher mass sum spectrum of 68.5 wt.% than CM-TD (63.2 wt.%). In addition, EG utilisation reportedly modified the properties of the support surface through the attachment of EG to the existing surface hydroxyl group of the support via hydrogen bonding [13]. Similarly, in this study, the ESM template is modified by the same phenomenon, via the addition of an extra functional group on the ESM surface. As mentioned previously, the ESM itself is composed of several surface functional groups, such as hydroxyl (–OH), thiol (–SH), carboxyl (–COOH), amino ($–NH_2$), and amide ($–CONH_2$) groups [17]. Therefore, in this study, the chelated metal compound was likely loaded onto the ESM surface and generated a CM-BT adsorbent with a smaller particle size than that of CM-TD after the calcination process.

Figures 2a–c show TEM and HRTEM images of CM-TD with SAED imaging. The HRTEM and SAED images (Figs. 2b, c) confirm that the lattice spacing of ~ 0.311 nm corresponds to the (111) plane of CeO_2. Furthermore, the decrease in the grain size of CM-BT compared to that of CM-TD, owing to the chelated cerium and magnesium ions, can be observed in Figs. 2a, d. However, the rod-like shape of the MgO particles observed in the FESEM image could not be observed in the TEM image. From the HRTEM images, the lattice spacing of CM-BT was measured to be the same as that of CM-TD; however, the SAED images confirm that the crystallite structure of CM-BT is different. In the SAED image (Fig. 2f), CM-BT exhibited a concentric ring, indicating a polycrystalline structure. Polycrystalline metal oxides are composed of many small crystals (crystallite/grains) with the same arrangement; however, the direction of atomic alignment varies randomly from one crystallite to the next [18–20]. Therefore, the crystalline structure and size of the prepared adsorbents were investigated further using XRD.

The XRD patterns of the CM adsorbents are shown in Fig. 3. The XRD profiles of CM-TD and CM-BT were comparable, and the diffraction peak intensities were influenced by the synthesis method used. Both adsorbents exhibited diffraction peaks at $2\theta = 28$, 33, 47, 56, 76, 88, and 95°, which can be assigned to the (111), (200), (220), (311), (331), (422), and (511) lattice planes, respectively, of a typical CeO_2 crystalline fluorite structure (JCPDS No. 34–0394) [21]. Only a few diffraction peaks corresponding to MgO (JCPDS No. 87–0653) were observed. They were located at $2\theta = 37°$ and 42°, which were assigned to the (111) and (200) lattice planes, respectively [22]. Moreover, several foreign peaks were observed in the 2θ range 5–45°, which may correspond to different crystal types of Mg compounds. In the close-up view of the XRD pattern, the peaks observed at 11.8°, 18.5°, 21.3°, and (25.66° and 36°) are assigned to the typical layered metal–oxygen sheet, $Mg(OH)_2$, $4MgCO_3.Mg(OH)_2.8H_2O$ (dypingite), and $MgCO_3{\cdot}3H_2O$ (nesquehonite), respectively (Fig. 3b) [22–24]. This shows that the rod-like structure of Mg, as observed in Fig. 1b, might be associated with Mg-related compounds, such as nesquehonite and dypingite, present in the adsorbent because the MgO crystal structure was not clearly observed in the XRD pattern of CM-BT [23, 25]. The average crystallite sizes of the prepared CM-TD and CM-BT were calculated to be 26.87 nm and 11.3 nm, respectively, using the Scherrer equation, with the peak parameter at $2\theta = 28°$ as the reference.

In addition, through Williamson–Hall (W–H) plotting (Fig. 3c), crystallite properties of both adsorbents have

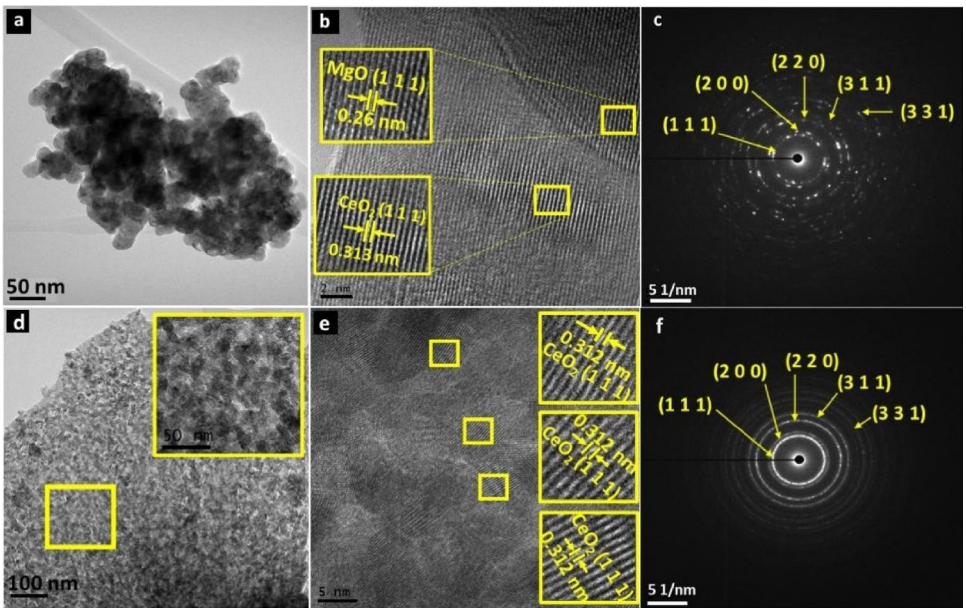

Fig. 2 TEM, HRTEM, and SAED images of; **a**–**c** CM-TD and **d**–**f** CM-BT

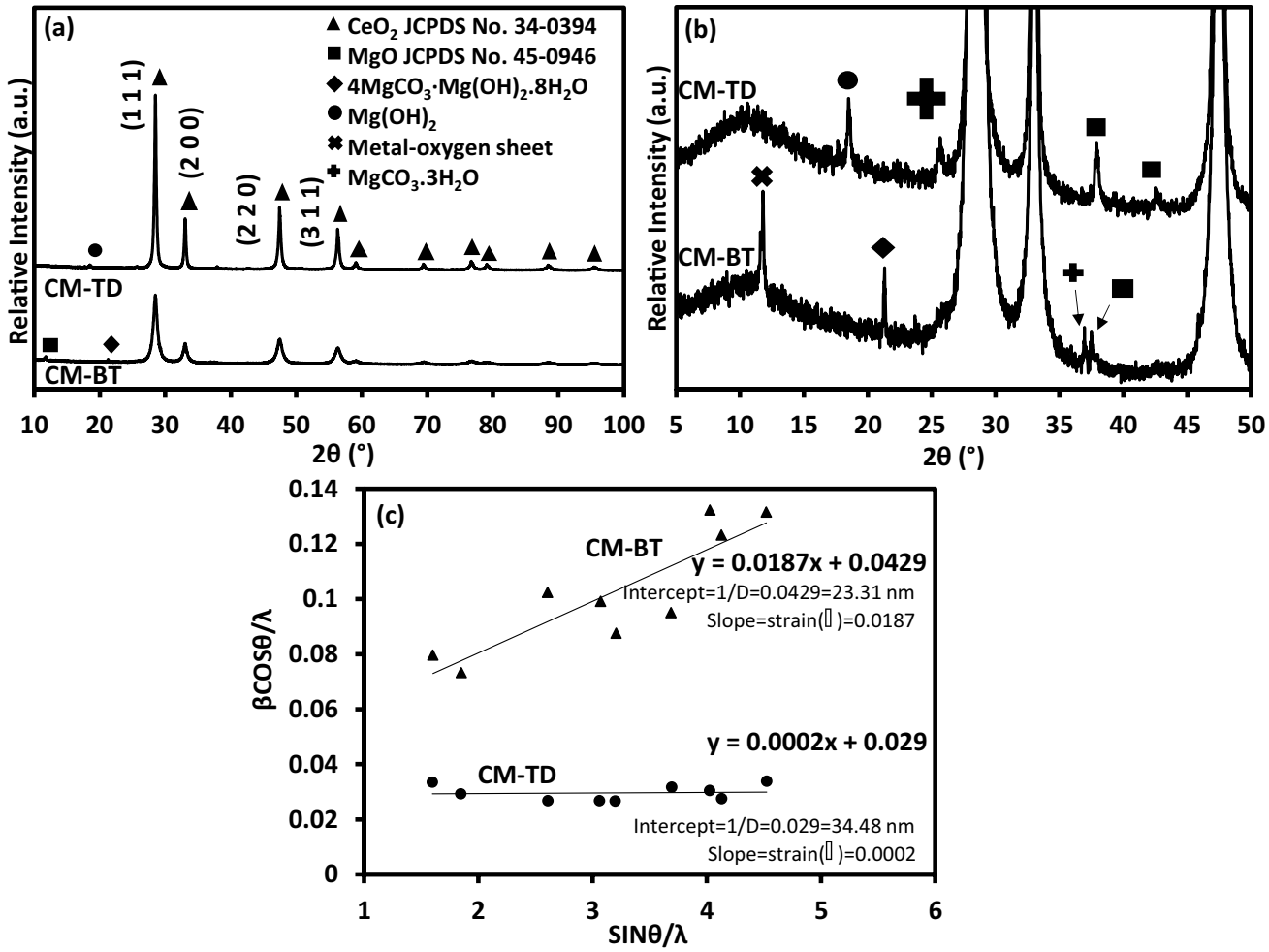

Fig. 3 **a**–**b** XRD pattern and **c** Williamson-Hall (W–H) plot of the CM adsorbent

been revealed differently than obtained using the Scherrer equation. The XRD peak broadening is controlled by both size and the lattice strain that could be appropriately expressed by Williamson–Hall (W–H) equation [26].

$$\frac{\beta \cos\theta}{\lambda} = \frac{1}{D} + \eta \frac{\sin\theta}{\lambda} \tag{3}$$

where λ is the x-ray wavelength if the equipment used (0.1589), θ is the peak position (radians), n is an order of refraction, λ is the x-ray wavelength (0.1589), β is the line broadening at half maximum intensity (FWHM) (radians), D is the effective crystallite size (nm), and η is the effective strain. The y-intercept and the slope of the linear fitting indicate the effective crystallite size (D) and effective strain (η), respectively. As depicted in Fig. 3c, W–H plotting revealed that CM demonstrated a larger crystallite size than Scherrer calculation. It was due to the strain term considered in W–H plotting [26]. Although, CM-BT still possess a smaller crystallite size with 23.31 nm than CM-TD (34.48 nm). In addition, besides the small crystallite size revealed by the CM-BT, it also shows a larger slope (strain, η) than CM-TD. The presence of a positive slope indicates that the adsorbent is under tensile strain, and the high strain was proposed to be the effect of grain boundary [27, 28]. According to Choudhury B. & Choudhury A., the generation of strain was associated with the presence of oxygen vacancy and defect (Ce^{3+}), hence expanding the lattice structure of the adsorbent nanoparticle. In addition, in the small crystallite size of ceria, the number of defects is higher than ceria with a larger crystallite size [26]. Thus, the utilisation of the ESM-templating method has resulted in the enhancement of the adsorbent's crystallinity structure, which might be a beneficial factor that contributes to the improvement of adsorbent CO_2 uptake capacity. Since the presence of high oxygen vacancy and defects site will contribute to the addition of the active binding site that promotes more binding of the CO_2 molecule on the adsorbent.

N_2 adsorption–desorption measurements were conducted to investigate the textural properties of the prepared CM

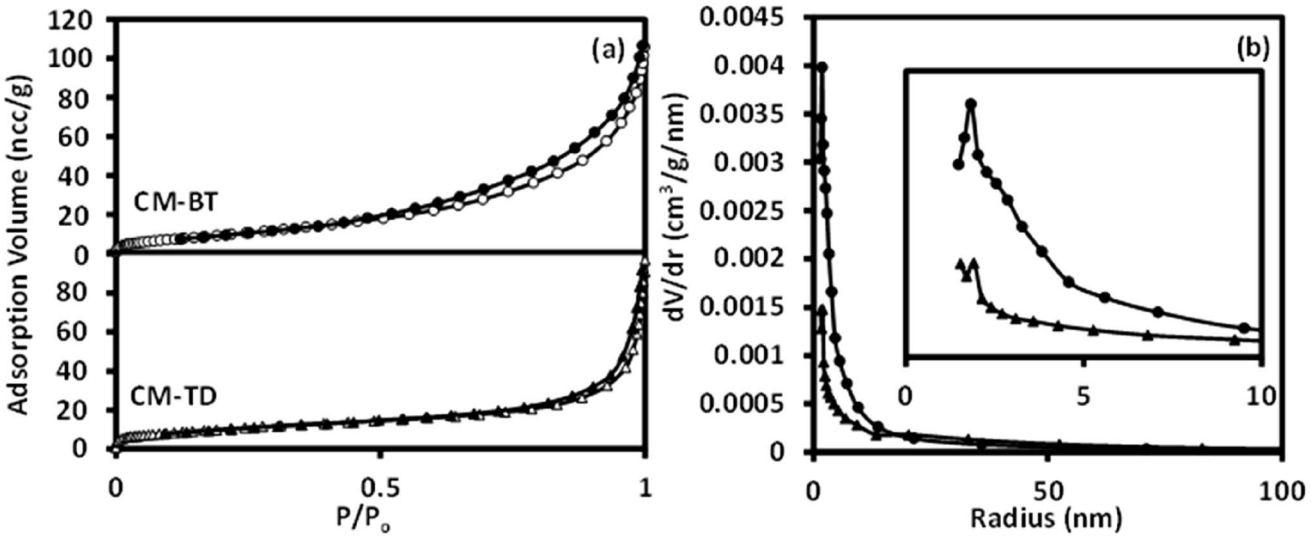

Fig. 4 **a** N_2 adsorption–desorption and **b** pore size distribution curve of the CM adsorbents

Table 1 Textural properties of the CM adsorbents

Sample	BET surface area (m^2/g)	BJH pore volume (cm^3/g)	Average pore diameter (nm)	Crystallite size (nm)
CM-TD	39	0.137	64	26.87
CM-BT	42	0.185	15	11.29

adsorbents. As shown in Fig. 4, both the CM adsorbents exhibited type IV isotherms with H3 hysteresis loops, indicating that they mainly possessed a mesoporous structure. The pores are mostly present as disordered slit pores resulting from the stacking of sheets or particles [29]. The hysteresis loops of the isotherms of both the samples were observed in the P/P_o range from 0.45 to 1.0 (Fig. 4a). The specific surface areas of the CM-TD and CM-BT adsorbents were 39 and 42 m^2/g, respectively, as listed in Table 1. This enhancement in the surface area of CM-BT might have resulted from the templating process of metal ion loading onto the ESM surface, which supposedly demonstrates the preservation of the fibrous ESM template structure, as reported previously [12, 30]. Furthermore, the Barrett–Joyner–Halenda (BJH) pore volume of CM-BT was higher than that of CM-TD.

The as-synthesised adsorbents were characterised via FTIR spectroscopy to understand whether the coordination bonding was affected by the different synthesis methods used. The FTIR spectra (Fig. 5a) of both the CM adsorbents show similar absorption peaks located at 3360 cm^{-1}, in the range 1107–1130 cm^{-1}, and below 650 cm^{-1}, which correspond to the stretching vibrations of the hydroxyl group (–OH), C–O, and metal–O bonds, respectively [7].

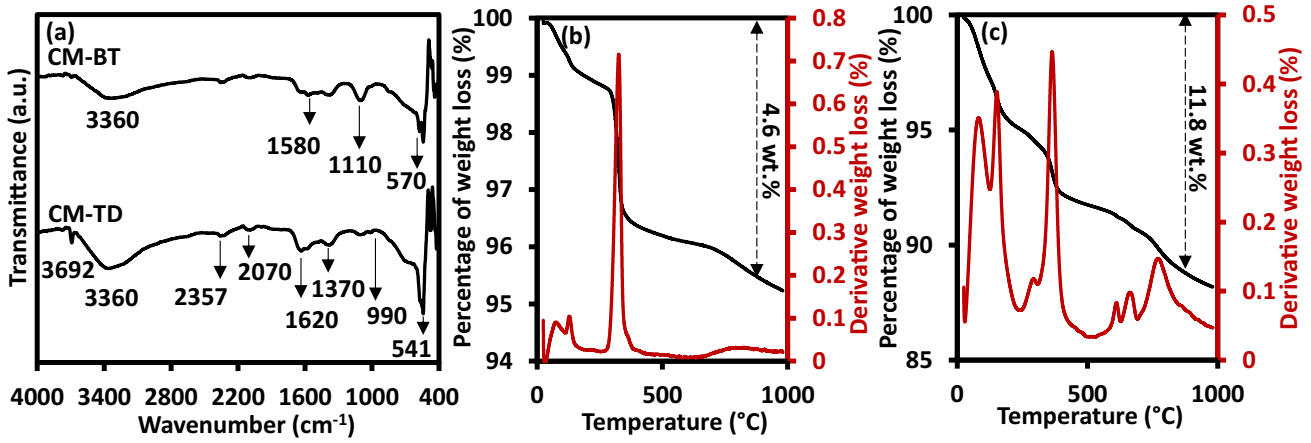

Fig. 5 **a** FTIR spectra of CM adsorbents and TGA-DTG curves of **b** CM-TD and **c** CM-BT

The bands present at 990 cm^{-1} and 3692 cm^{-1} in the FTIR spectrum of the CM-TD adsorbent are attributed to the bending mode of the bridging and stretching vibrations, respectively, of the surface hydroxyl group, thereby supporting the presence of a peak corresponding to $Mg(OH)_2$ in the XRD spectrum of CM-TD (Fig. 3) [31]. The intense 1110 cm^{-1} band observed in the CM-BT spectra might correspond to a carbon-based compound, which may be associated with the carbonaceous residue present in the adsorbent from the ESM used [32]. As reported by He et al., at calcination temperatures in the range 773–1273 K, ESMs undergo a slow and continuous degradation process [11]. Thus, because CM-BT was prepared at 773 K, the carbonaceous residue of the ESM remained in the CM-BT.

Furthermore, the band corresponding to CO_2 adsorbed from the surrounding atmosphere was observed for both adsorbents. Several peaks corresponding to carbon-related species are present in the FTIR spectra of both the adsorbents, which are located at 1370, 1580, 2070, and approximately 2360 cm^{-1} [33–36]. The bands at 1370 and 1580 cm^{-1} correspond to CO_3^{2-} and C=C bonds, respectively [34, 35]. Moreover, the CM adsorbent exhibited a band at 2070 cm^{-1}, which is usually attributed to the C–O stretching of carbon monoxide bound to surface of the metal oxide adsorbent [36]. Furthermore, both the adsorbents displayed a band at 1635 cm^{-1}, which is ascribed to the bending mode of the hydroxyl groups of adsorbed water [37]. This is attributed to the attachment of water to the Brønsted acid sites of the adsorbents [38]. Although both the adsorbents exhibited similar peaks throughout the spectra, their intensities were slightly different.

The thermal decomposition behaviour of the CM adsorbents is shown in Figs. 5b, c. The TGA data exhibited a slightly different weight loss curve for both the CM adsorbents. The differences might be attributed to the different chemical compounds present in the sample. However, the temperature range of the degradation stages was almost the same. Both adsorbents exhibited the first stage of degradation at a temperature below 523 K, corresponding to residual moisture removal, in which the weight loss of CM-BT was higher than that of CM-TD. In the second stage of degradation, a sharp DTG peak was observed for the both samples, which corresponds to organic residue degradation. This degradation resulted in the liberation of CO_2, H_2O, and NO_2 gases. However, both the adsorbents exhibited slightly different temperature ranges: the second stage of degradation of CM-BT occurred at 523–723 K, whereas that of CM-TD occurred across a wider temperature range of 523–823 K.

The high derivative weight loss peak of CM-TD indicates that it contains a higher organic residue than CM-BT. In the third stage of the degradation behaviour, both the adsorbents demonstrated characteristics in contrast to those in the second stage. CM-BT exhibited a higher weight loss (3.2 wt.%) than CM-TD, which only exhibited less than 1% weight loss in the third stage. This indicates that CM-BT contained a higher amount of carbonaceous residue than CM-TD, owing to the ESM template used. This is because the sample was prepared at a calcination temperature of 723 K, whereas ESM has been reported to be completely decomposed only at 923 K [39]. Therefore, ESM carbonaceous residue is present in the adsorbent, which is in good agreement with the FTIR spectra.

3.2 CO_2-TPD of the synthesised CM-TD and CM-BT adsorbents

Adsorbent surface basicity has been reported to play a vital role in achieving a high CO_2 uptake capacity. This can be evaluated through the temperature-programmed desorption of CO_2 (CO_2-TPD). The deconvoluted TPD curves generated with respect to temperature (Fig. 7) indicate that the signal corresponds to the CO_2 desorbed from the active site of the adsorbent. The basicity strength can be quantified as the area under the deconvoluted TPD curve. The higher the desorption temperature, the stronger the strength of the base site of the adsorbent. This can be explained by understanding the mechanism of CO_2 attachment to the adsorbent surface. During the carbonation process, the attachment of CO_2 to the Brønsted basic site (surface hydroxyl groups) of the adsorbent generates bicarbonate species. The hydroxyl group in the adsorbent is categorised as the weak attachment site of the adsorbent, and the desorption of CO_2 from this site occurred at temperatures below 473 K.

Moreover, CO_2 can attach to the Lewis acid–base sites of the adsorbent (medium strength), resulting in the formation of bidentate carbonate species. This reaction occurred between the CO_2 molecule and the $Mg^{2+}/Ce^{3+}/Ce^{4+}$ and O^{2-} sites of the adsorbent [40, 41]. Furthermore, the presence of defect ions can induce the formation of this medium-strength binding site. Defect ions are generated by the reduction in Ce ions from Ce^{4+} to Ce^{3+} ions. The reduction in Ce^{4+} to Ce^{3+} cations is explained by the decrease in the number of O^{2-} anions surrounding Ce^{4+} cations from eight to seven anions, thereby creating oxygen vacancies [42]. Finally, the strongest interaction during carbonation resulted in the formation of monodentate carbonate species [41]. This chemisorption interaction occurred between CO_2 and the low-coordinated oxygen (O^{2-}) defect site and resulted in the formation of CO_3^{2-} [40]. A schematic of the formation of carbonate species during carbonation is shown in Fig. 6.

Composite CeO_2–MgO adsorbents have been reported to possess better surface basicity than single-metal adsorbents (MgO and CeO_2) [9, 43, 44]. As previously observed in the FTIR spectra, the CM adsorbents displayed several bands corresponding to atmospheric CO_2 attachment on the sample, thereby demonstrating high surface reactivity.

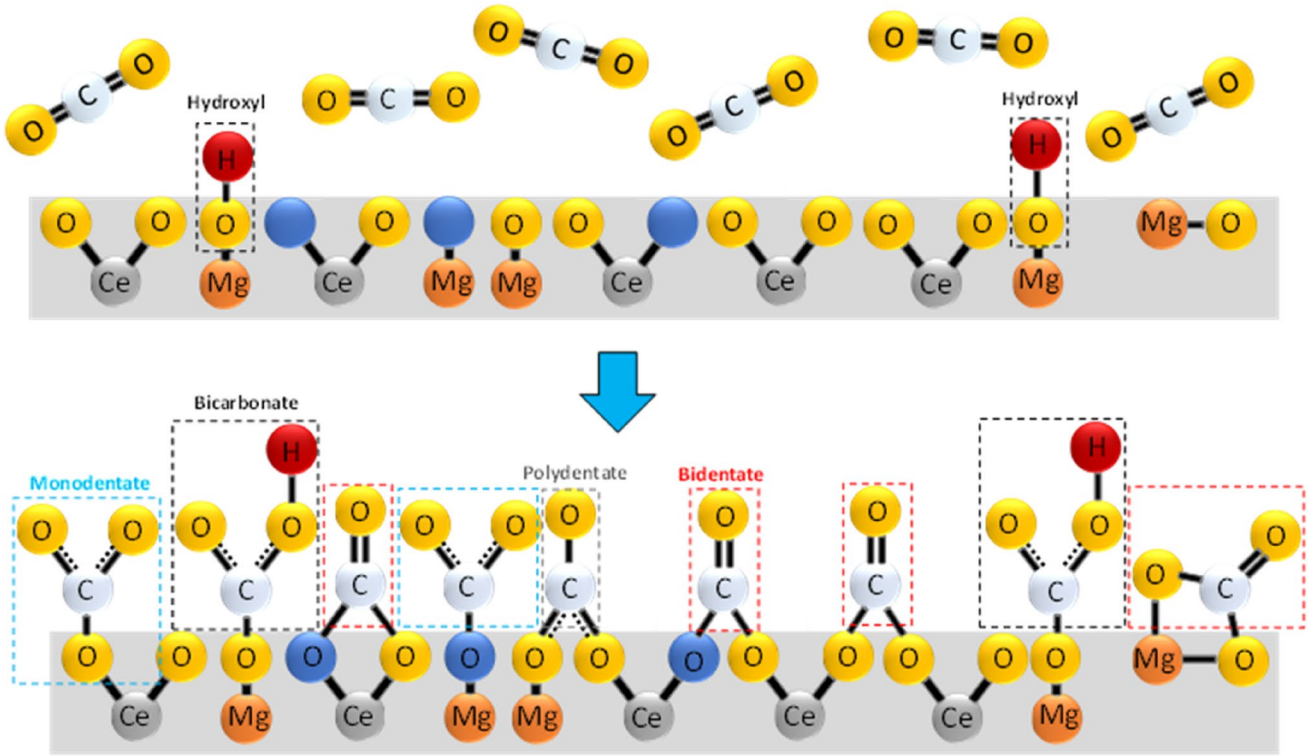

Fig. 6 The proposed mechanism of carbonate species formation on the surface of the CeO_2–MgO composite during CO_2 adsorption

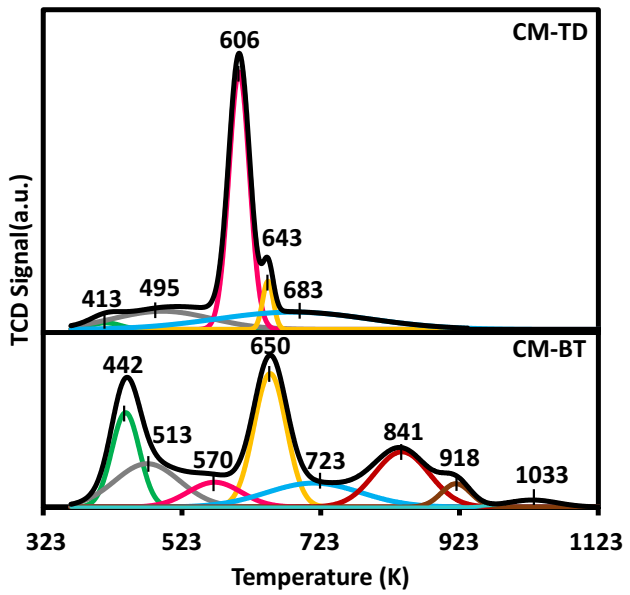

Fig. 7 Deconvoluted CO_2-TPD profiles of the CM-TD and CM-BT adsorbents

Therefore, further evaluation of the surface basic strength of both the adsorbents was conducted. The CO_2-TPD profiles of both the CM adsorbents are shown in Fig. 7. Generally, the desorbed CO_2 peak has been observed at temperatures below 473 K and in the ranges 473–573 K and 573–873 K, corresponding to the desorption of CO_2 from the weak, medium, and strong base sites, respectively [45, 46]. Owing to the improved structural properties of CM-BT compared to those of CM-TD, the peaks at 413, 495, and 606 K of the deconvoluted curve of CM-TD were shifted to a slightly higher temperature in the TPD profile of CM-BT. This implies a stronger basic property that results in a higher CO_2 capture capacity [41].

Considering the differences in the CO_2-TPD profiles of the adsorbents, it is useful to understand the contribution of the carbonate species to the desorption of CO_2 at the respective temperatures. At a low desorption temperature, the desorbed CO_2 corresponds to the hydrogen carbonate/bicarbonate species [47]. As the temperature reached 573 K, desorbed CO_2 was associated with the formation of monodentate carbonate and bidentate carbonate species [48]. As the temperature further increased to 773 K, the desorbed CO_2 is associated with the carbonate species (polydentate carbonate species) formed on the CeO_2 surface [49].

The desorption of CO_2 from CeO_2 and MgO generally occurs in the temperature range of 323 to 873 K [45, 46]. The TPD profile of CM-BT shows several peaks at high temperatures (> 773 K). Therefore, it is interesting that the carbonate species contributes to CO_2 desorption at temperatures greater than 773 K. This TPD profile obtained for CM-BT

(Fig. 7) matches with that of desorbed CO_2 molecules from the carbonate species formed on the strong base site of MgO, as reported by Gao et al. [41]. Furthermore, it is well known that the desorption of CO_2 at temperatures greater than 573 K corresponds to desorption from monodentate carbonate species. The strength of monodentate carbonate varies, which correlates with the coordination number and electronegativity of the coordination metal ions. A strong basic nature corresponds to a high electron density of O^{2-} exhibited by a metal oxide with few coordinated O^{2-} ions and a low electronegativity of metal ions [41]. Therefore, CM-BT possesses diverse strong-basic sites, which results in the desorption of CO_2 from monodentate carbonate at a different and higher temperature than that from CM-TD.

The amount of CO_2 desorbed was quantified from the area under the deconvoluted curve at the respective temperature. As listed in Table 2, CM-BT exhibited a higher amount of desorbed CO_2 at every basic site, indicating an abundance of active sites, thereby resulting in a higher total amount of desorbed CO_2 than that from CM-TD. The total amount of CO_2 desorbed from CM-TD and CM-BT was calculated to be 1.472 and 1.974 mmol/g, respectively. Therefore, the diversity of strong basic sites could be a factor, in addition to the decent structural properties generated by the ESM bio-templating method, contributing to the enhancement of the CO_2 uptake capacity of CM-BT.

The amount of CO_2 desorbed was calculated from the area under the peaks of the deconvoluted CO_2-TPD profiles in Fig. 7.

Values in parentheses are the percentages of the areas under each deconvoluted peak in the CO_2-TPD profiles shown in Fig. 7.

Table 2 Quantification of the CO_2-TPD profiles of the CM adsorbent

Adsorbent	Adsorption site	Amount of CO_2 desorbed (mmol/g)	Total (mmol/g)
CM-TD	Weak site (< 473 K)	0.193 (1.88%)	1.472
	Medium site (473–573 K)	0.275 (16.54%)	
	Strong site (> 573 K)	1.004 (81.58%)	
CM-BT	Weak site (< 473 K)	0.323 (15.05%)	1.974
	Medium site (473–573 K)	0.332 (23.62%)	
	Strong site (> 573 K)	1.319 (61.33%)	

3.3 CO_2 uptake capacity of CM-BT and CM-TD adsorbents

CO_2 adsorption testing was conducted to evaluate the effect of the physicochemical properties of the enhanced adsorbent on CO_2 uptake performance. The tests were performed under CO_2 flow and ambient conditions. As shown in Fig. 8a, CM-BT exhibited a higher CO_2 uptake capacity of 5.70 mmol CO_2/g, which was approximately 2.5 times higher than that of CM-TD. Hence, the enhancement of the physicochemical properties of CM-BT, such as surface area and pore volume, induced a high active site exposure in the adsorbent. Furthermore, CM-BT demonstrated an abundance of basic sites comprising weak-, medium-, and diverse strong-basic sites, which resulted in a higher carbonate formation than observed in CM-TD. In addition, the basic sites of CM-BT were likely influenced by the presence of carbonaceous residue in the adsorbent. The remaining

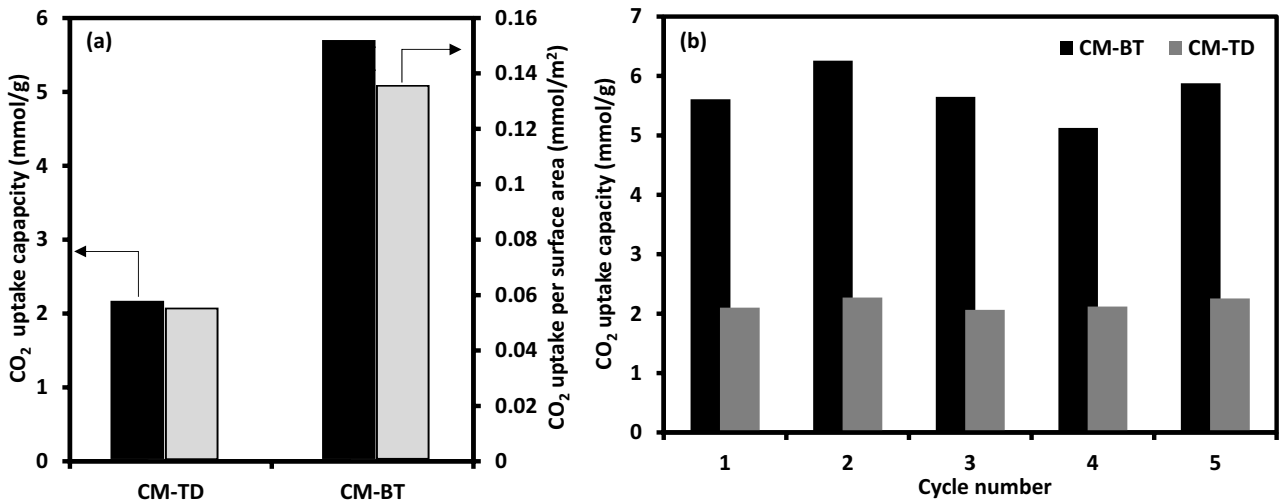

Fig. 8 **a** CO_2 uptake capacity and **b** CO_2 adsorption–desorption cyclic performance of the CM adsorbents

carbonaceous residue contributes to the formation of abundant oxygen defects and the resulting strong basic sites [43].

Additionally, this composite CM-BT adsorbent exhibited higher CO_2 uptake capacity than those reported previously for single-metal (MgO and CeO_2 individually) and composite CeO_2–MgO adsorbents [43, 49–52]. The CM-BT composite adsorbent demonstrated better uptake capacity than those reported for MgO and CeO_2 in the studies conducted by Tuan et al. and Azmi et al. on fabricated MgO and CeO_2, respectively [50, 52]. Although both the single-metal adsorbents were reported as having a higher surface area than that of CM-BT, the composite CM-BT adsorbent exhibited an improved CO_2 uptake capacity owing to oxygen vacancies that create more active sites on the adsorbent. In addition, at low adsorption temperatures (< 423 K), CM-BT demonstrated an enhanced CO_2 uptake capacity compared to that of the composite CeO_2–MgO (MgCe5%) adsorbent reported by Jin et al., which exhibited an uptake capacity of only 2.36 mmol CO_2/g [43]. Furthermore, this result can be attributed to the high surface reactivity of CM-BT, as CM-BT exhibited more peaks corresponding to CO_2 desorbed from the adsorbent's active site (Fig. 7). The previously reported MgCe5% displayed only three peaks corresponding to CO_2 desorbed from the adsorbent's weak-, medium-, and strong base sites. Notably, similar to CM-BT, MgCe5% also reportedly contained a small amount of carbonaceous residue, which might influence its performance. Therefore, the high surface reactivity of the adsorbent, indicated by the abundance of its active base sites, plays a significant role in contributing to its high CO_2 uptake capacity.

The practicability of the prepared CM adsorbents was evaluated with five adsorption–desorption cycle testing. As depicted in Fig. 8b, throughout the 5-cycle, both CM adsorbents demonstrated quite wobbly CO_2 uptake capacity. At the initial CO_2 adsorption process, CM-BT exhibited an uptake capacity of 5.61 mmol/g and 5.88 mmol/g on the fifth cycle. Although, the highest uptake capacity of CM-BT was demonstrated on the second cycle with 6.30 mmol/g. The same trend was also observed on CM-TD adsorbent but with a smaller uptake capacity than CM-BT. This shows that despite having slightly unsteady uptake capacity, CM-BT still exhibited more than two times higher uptake than CM-TD on every cycle.

4 Conclusions

In summary, a mesoporous CeO_2–MgO (CM-BT) composite was successfully fabricated via ESM-templating. The utilisation of ESM bio-templating improved the physicochemical properties of CM-BT. The CM-BT adsorbent exhibited a larger surface area and pore volume than those of CM-TD. However, CM-BT did not display any preservation of the ESM fibrous structure. Furthermore, the CM-BT adsorbent comprised a greater number of strong basic sites featuring O^{2-} of diverse strengths, and weak and medium sites than those of CM-TD. Such enhanced physicochemical properties resulted in a CO_2 uptake capacity of 5.70 mmol CO_2/g, which is 2.5 times higher than that of CM-TD and higher than that of a previously reported composite CeO_2–MgO adsorbent. Therefore, bio-templating is a promising approach for fabricating adsorbents with excellent physicochemical properties to enhance the adsorbent uptake capacity. Thus, there is immense scope for further investigation into the potential utilisation of other natural materials as templates to fabricate excellent adsorbents through this method.

Acknowledgements This work was supported by the Universiti Teknologi Malaysia (Grant No. 08G94) and Ministry of Higher Education Malaysia through Fundamental Research Grant Scheme (FRGS) Grant No. FRGS/1/2019/STG07/UTM/02/8 (Grant No. 5F217).

References

1. D. Sangroya, J.K. Nayak, Factors influencing buying behaviour of green energy consumer. J. Clean. Prod. **151**, 393–405 (2017)
2. E. Abbasi, A. Hassanzadeh, J. Abbasian, Regenerable MgO-based sorbent for high temperature CO_2 removal from syngas: 2 Two-zone variable diffusivity shrinking core model with expanding product layer. Fuel **105**, 128–134 (2013)
3. Y. Guo, C. Tan, P. Wang, J. Sun, W. Li, C. Zhao, P. Lu, Magnesium-based basic mixtures derived from earth-abundant natural minerals for CO_2 capture in simulated flue gas. Fuel **243**, 298–305 (2019)
4. A. Azmi, M. Aziz, Mesoporous adsorbent for CO_2 capture application under mild condition: a review. J. Environ. Chem. Eng. **7**, 103022 (2019)
5. A.H. Ruhaimi, M.A.A. Aziz, A.A. Jalil, Magnesium oxide-based adsorbents for carbon dioxide capture: current progress and future opportunities. J. CO_2 Util. **43** (2021) 101357.
6. M. Khraisheh, S. Mukherjee, A. Kumar, F. Al Momani, G. Walker, M.J. Zaworotko, An overview on trace CO_2 removal by advanced physisorbent materials. J. Environ. Manag. **255** (2020) 109874.
7. P. Li, Y. Lin, R. Chen, W. Li, Construction of a hierarchical-structured MgO-carbon nanocomposite from a metal–organic complex for efficient CO_2 capture and organic pollutant removal. Dalton Trans. **49**, 5183–5191 (2020)
8. L. Liu, J. Shi, X. Zhang, J. Liu, Flower-like Mn-doped CeO_2 Microstructures: synthesis, characterizations, and catalytic properties. J. Chem. **2015**, 254750 (2015)
9. H. Yu, X. Wang, Z. Shu, M. Fujii, C. Song, Al_2O_3 and CeO_2-promoted MgO sorbents for CO_2 capture at moderate temperatures. Front. Chem. Sci. Eng. **12**(1), 83–93 (2018)
10. A. Hanif, S. Dasgupta, A. Nanoti, Facile synthesis of high-surface-area mesoporous MgO with excellent high-temperature CO_2 adsorption potential. Ind. Eng. Chem. Res. **55**(29), 8070–8078 (2016)
11. X. He, D.P. Yang, X. Zhang, M. Liu, Z. Kang, C. Lin, N. Jia, R. Luque, Waste eggshell membrane-templated CuO-ZnO nanocomposites with enhanced adsorption, catalysis and antibacterial properties for water purification. Chem. Eng. J. **369**, 621–633 (2019)

12. N. Preda, A. Costas, M. Enculescu, I. Enculescu, Biomorphic 3D fibrous networks based on ZnO, CuO and ZnO–CuO composite nanostructures prepared from eggshell membranes. Mater. Chem. Phys. **240**, 122205 (2020)
13. T. Osaki, Effect of ethylene glycol on structure, thermal stability, oxygen storage capacity, and catalytic CO and CH_4 oxidation activities of binary CeO_2–Al_2O_3 and ternary CeO_2–ZrO_2–Al_2O_3 cryogels. J. Sol-Gel. Sci. Technol. **82**(1), 133–147 (2017)
14. N. Abdullah, N. Osman, S. Hasan, O. Hassan, Chelating agents role on thermal characteristics and phase formation of modified cerate-zirconate via sol-gel synthesis route. Int. J. Electrochem. Sci **7**, 9401–9409 (2012)
15. P. Li, R. Chen, Y. Lin, W. Li, General approach to facile synthesis of MgO-based porous ultrathin nanosheets enabling high-efficiency CO_2 capture. Chem. Eng. J. **404**, 126459 (2021)
16. C. Yang, X. Song, S. Sun, Z. Sun, J. Yu, Effects of sodium dodecyl sulfate on the oriented growth of nesquehonite whiskers. Adv. Powder Technol. **24**(3), 585–592 (2013)
17. A. Mittal, M. Teotia, R. Soni, J. Mittal, Applications of egg shell and egg shell membrane as adsorbents: a review. J. Mol. Liq. **223**, 376–387 (2016)
18. G. Yang, S.J. Park, Deformation of Single Crystals, Polycrystalline Materials, and Thin Films: A Review. Materials (Basel) **12**(12) (2019) 2003.
19. G. Kaur, A. Mitra, K.L. Yadav, Pulsed laser deposited Al-doped ZnO thin films for optical applications. Prog. Natural Sci.: Mater. Int. **25**(1), 12–21 (2015)
20. R.F. Egerton, Physical principles of electron microscopy, 2nd edn. Springer, pp. 93–124 (2005)
21. Z. Feng, Q. Ren, R. Peng, S. Mo, M. Zhang, M. Fu, L. Chen, D. Ye, Effect of CeO_2 morphologies on toluene catalytic combustion. Catal. Today **332**, 177–182 (2019)
22. A. Vedyagin, A. Bedilo, I. Mishakov, E. Shuvarakova, Study of MgO transformation into MgF_2 in the presence of CF_2Cl_2•. J. Serb. Chem. Soc. **82**, 37–37 (2017)
23. Q. Chen, T. Hui, H. Sun, T. Peng, W. Ding, Synthesis of magnesium carbonate hydrate from natural talc. Open Chem. **18**(1), 951–961 (2020)
24. S. Yousefi, B. Ghasemi, M. Tajally, A. Asghari, Optical properties of MgO and $Mg(OH)_2$ nanostructures synthesized by a chemical precipitation method using impure brine. J. Alloy. Compd. **711**, 521–529 (2017)
25. A. Pilarska, I. Linda, M. Wysokowski, D. Paukszta, T. Jesionowski, Synthesis of $Mg(OH)_2$ from magnesium salts and NH_4OH by direct functionalisation with poly (ethylene glycols). Physicochem. Probl. Miner. Process **48**(2), 631–643 (2012)
26. B. Choudhury, A. Choudhury, Ce^{3+} and oxygen vacancy mediated tuning of structural and optical properties of CeO_2 nanoparticles. Mater. Chem. Phys. **131**(3), 666–671 (2012)
27. P. Muhammed Shafi, A. Chandra Bose, Impact of crystalline defects and size on X-ray line broadening: a phenomenological approach for tetragonal SnO_2 nanocrystals. AIP Adv. **5**(5) (2015) 057137.
28. K.M. Prabu, S. Perumal, Micro strain and morphological studies of anatase and rutile phase TiO_2 nanocrystals prepared via sol-gel and solvothermal method—a comparative study. IJSRSET **1**, 299–304 (2015)
29. Y. Guo, C. Tan, P. Wang, J. Sun, W. Li, C. Zhao, P. Lu, Structure-performance relationships of magnesium-based CO_2 adsorbents prepared with different methods. Chem. Eng. J. **379**, 122277 (2020)
30. H. He, P. Yang, CeO_2/NiO nanostructures created using eggshell membrane towards enhanced catalytic activity. J. Nanosci. Nanotechnol. **18**(1), 340–346 (2018)
31. C. Azer, A.R. Ramadan, G. Ghaly, J. Ragai, Preparation and characterization of cobalt aluminate spinels $CoAl_2O_4$ doped with magnesium oxide. Adsorpt. Sci. Technol. **30**(5), 399–407 (2012)
32. M. Poletto, A.J. Zattera, R.M.C. Santana, Structural differences between wood species: evidence from chemical composition, FTIR spectroscopy, and thermogravimetric analysis. J. Appl. Polym. Sci. **126**(S1), E337–E344 (2012)
33. J.M.A. Almeida, P.E.C. Santos, L.P. Cardoso, C.T. Meneses, A simple method to obtain Fe-doped CeO_2 nanocrystals at room temperature. J. Magn. Magn. Mater. **327**, 185–188 (2013)
34. J. Safaei-Ghomi, F.S. Bateni, P. Babaei, CeO2/CuO@ N-GQDs@ NH2 nanocomposite as a high-performance catalyst for the synthesis of benzo [g] chromenes. Appl. Organomet. Chem. **34**(7), e5657 (2020)
35. L.F. Nascimento, J.F. Lima, P.C. de Sousa Filho, O.A. Serra, Effect of lanthanum loading on nanosized CeO_2-ZnO solid catalysts supported on cordierite for diesel soot oxidation. J. Environ. Sci. **73** (2018) 58–68.
36. O. Krauth, G. Fahsold, A. Pucci, Asymmetric line shapes and surface enhanced infrared absorption of CO adsorbed on thin iron films on MgO(001). J. Chem. Phys. **110**(6), 3113–3117 (1999)
37. C.S. Riccardi, R.C. Lima, M.L. dos Santos, P.R. Bueno, J.A. Varela, E. Longo, Preparation of CeO_2 by a simple microwave–hydrothermal method. Solid State Ionics **180**(2), 288–291 (2009)
38. D.R. Mullins, P.M. Albrecht, F. Calaza, Variations in reactivity on different crystallographic orientations of cerium oxide. Top. Catal. **56**(15–17), 1345–1362 (2013)
39. U. Sabu, M. Rashad, G. Logesh, K. Kumar, M. Lodhe, M. Balasubramanian, Development of biomorphic alumina using egg shell membrane as bio-template. Ceram. Int. **44**(5), 4615–4621 (2018)
40. D. Ochs, M. Brause, B. Braun, W. Maus-Friedrichs, V. Kempter, CO_2 chemisorption at Mg and MgO surfaces: a study with MIES and UPS (He I). Surf. Sci. **397**(1), 101–107 (1998)
41. W. Gao, T. Zhou, Q. Wang, Controlled synthesis of MgO with diverse basic sites and its CO_2 capture mechanism under different adsorption conditions. Chem. Eng. J. **336**, 710–720 (2018)
42. S. Kumar, M. Srivastava, J. Singh, S. Layek, M. Yashpal, A. Materny, A.K. Ojha, Controlled synthesis and magnetic properties of monodispersed ceria nanoparticles. AIP Adv. **5**(2), 027109 (2015)
43. S. Jin, G. Bang, L. Liu, C.-H. Lee, Synthesis of mesoporous MgO–CeO_2 composites with enhanced CO_2 capture rate via controlled combustion. Microporous Mesoporous Mater. **288**, 109587 (2019)
44. P. Liu, H. Chen, H. Yu, X. Liu, R. Jiang, X. Li, S. Zhou, Oxygen vacancy in magnesium/cerium composite from ball milling for hydrogen storage improvement. Int. J. Hydrogen Energy **44**(26), 13606–13612 (2019)
45. S. Jin, G. Bang, C.H. Lee, Unusual morphology transformation and basicity of magnesium oxide controlled by ageing conditions and its carbon dioxide adsorption. J. CO_2 Util. **41** (2020) 101273.
46. M. Alsawalha, Characterization of acidic and basic properties of heterogeneous catalysts by test reactions, Ph.D. Thesis. University of Oldenburg: Oldenburg, Germany (2004).
47. K. Yoshikawa, H. Sato, M. Kaneeda, J.N. Kondo, Synthesis and analysis of CO_2 adsorbents based on cerium oxide. J. CO_2 Util. **8** (2014) 34–38.
48. W. Janssens, E.V. Makshina, P. Vanelderen, F. De Clippel, K. Houthoofd, S. Kerkhofs, J.A. Martens, P.A. Jacobs, B.F. Sels, Ternary Ag/MgO-SiO_2 catalysts for the conversion of ethanol into butadiene. Chemsuschem **8**(6), 994–1008 (2015)
49. K. Yoshikawa, M. Kaneeda, H. Nakamura, Development of Novel CeO_2-based CO_2 adsorbent and analysis on its CO_2 adsorption and desorption mechanism. Energy Procedia **114**, 2481–2487 (2017)

50. V.A. Tuan, C.H. Lee, Preparation of rod-like MgO by simple precipitation method for CO_2 capture at ambient temperature. Vietnam J. Chem. **56**(2), 197–202 (2018)
51. K. Ho, S. Jin, M. Zhong, A.T. Vu, C.H. Lee, Sorption capacity and stability of mesoporous magnesium oxide in post-combustion CO_2 capture. Mater. Chem. Phys. **198**, 154–161 (2017)
52. A.A. Azmi, A.H. Ruhaimi, M.A.A. Aziz, Efficient 3-aminopropyltrimethoxysilane functionalised mesoporous ceria nanoparticles for CO_2 capture. Mater. Today Chem. **16**, 100273 (2020)